Metzger, S., Schurr, B., Ratschbacher, L., Sudhaus, H., Kufner, S.-K., Schöne, T., Zhang, Y., Perry, M., Bendick, R. (2017): The 2015 Mw7.2 Sarez strike-slip earthquake in the Pamir interior: Response to the underthrusting of India's western promontory. - *Tectonics*, *36*, 11, pp. 2407—2421.

DOI: http://doi.org/10.1002/2017TC004581

AGU PUBLICATIONS

Tectonics

RESEARCH ARTICLE
10.1002/2017TC004581

Key Points:
- SAR data and modeling reveal a right-stepping, near-vertical, ~80 km long rupture along the Sarez-Karakul fault with sinistral slip of up to 3.1 m
- Surface breaks in frozen ground record fault segmentation, en échelon secondary structures, mass movements, and up to 2 m sinistral offset
- Faulting is probably driven by northward advance of the northwestern tip of underthrusting Indian mantle lithosphere

Supporting Information:
- Supporting Information S1

Correspondence to:
S. Metzger,
metzger@gfz-potsdam.de

Citation:
Metzger, S., Schurr, B., Ratschbacher, L., Sudhaus, H., Kufner, S.-K., Schöne, T., … Bendick, R. (2017). The 2015 M_w7.2 Sarez strike-slip earthquake in the Pamir interior: Response to the underthrusting of India's western promontory. *Tectonics*, *36*, 2407–2421. https://doi.org/10.1002/2017TC004581

Received 23 MAR 2017
Accepted 29 AUG 2017
Accepted article online 2 OCT 2017
Published online 6 NOV 2017

The 2015 M_w7.2 Sarez Strike-Slip Earthquake in the Pamir Interior: Response to the Underthrusting of India's Western Promontory

Sabrina Metzger[1], Bernd Schurr[1], Lothar Ratschbacher[2], Henriette Sudhaus[3], Sofia-Katerina Kufner[1], Tilo Schöne[4], Yong Zhang[5], Mason Perry[6], and Rebecca Bendick[6]

[1]Lithosphere Dynamics, GFZ German Research Centre for Geosciences, Potsdam, Germany, [2]Geologie, TU Bergakademie Freiberg, Freiberg, Germany, [3]Institute of Geosciences, Christian-Albrechts-University, Kiel, Germany, [4]Geodetic Hazard MonitoringGFZ German Research Centre for Geosciences, Potsdam, Germany, [5]School of Earth and Space Sciences, Peking University, Beijing, China, [6]Department of Geosciences, University of Montana, Missoula, MT, USA

Abstract The Pamir orogen, Central Asia, is the result of the ongoing northward advance of the Indian continent causing shortening inside Asia. Geodetic and seismic data place the most intense deformation along the northern rim of the Pamir, but the recent 7 December 2015, M_w7.2 Sarez earthquake occurred in the Pamir's interior. We present a distributed slip model of this earthquake using coseismic geodetic data and postseismic field observations. The earthquake ruptured an ~80 km long, subvertical, sinistral fault consisting of three right-stepping segments from the surface to ~30 km depth with a maximum slip of three meters in the upper 10 km of the crust. The coseismic slip model agrees well with en échelon secondary surface breaks that are partly influenced by liquefaction-induced mass movements. These structures reveal up to 2 m of sinistral offset along the northern, low-offset segment of modeled rupture. The 2015 event initiated close to the presumed epicenter of the 1911 M_w ~7.3 Lake Sarez earthquake, which had a similar strike-slip mechanism. These earthquakes highlight the importance of NE trending sinistral faults in the active tectonics of the Pamir. Strike-slip deformation accommodates shear between the rapidly northward moving eastern Pamir and the Tajik basin in the west and is part of the westward (lateral) extrusion of thickened Pamir plateau crust into the Tajik basin. The Sarez-Karakul fault system and the two large Sarez earthquakes likely are crustal expressions of the underthrusting of the northwestern leading edge of the Indian mantle lithosphere beneath the Pamir.

Plain Language Summary The Pamir mountains in Central Asia are being piled up by the northward advancing Indian continent. Nowadays most of the deformation occurs at the Pamir's rim, but on 7 December 2015, a large earthquake struck the interior of this mountain range (magnitude 7). We use radar satellite data with centimeter accuracy to measure the coseismic displacement of this earthquake and find that an 80 km long segment of the Sarez-Karakul fault was ruptured. This fault splits the Pamir in a western and eastern part. Our geologists, who visited the area 9 months after the earthquake, confirmed our observations and further reported that the rupture was heavily damped at the surface by permafrost. The area was already once struck by a large earthquake in 1911. The question arises if also this event activated the Sarez-Karakul fault, as this fault is the only known large structure in the Pamir's interior. But the center of the Pamir deforms only little, and it is unlikely that this fault ruptures twice in 100 years. Finally, we show that both earthquakes occurred directly on top of the Indian promontory bulldozing into the Asian crust underneath the Pamir.

1. Introduction

The Pamir, situated northwest of the Tibetan Plateau, is part of the India-Asia collision zone (Figure 1). The region is seismically active producing magnitude >6 earthquakes approximately every 10 years. Over the last 50 years, those occurred mainly along the Pamir's northern perimeter, the Pamir thrust system, which accommodates 13–19 mm/yr of the India-Asia convergence (Ischuk et al., 2013; Zubovich et al., 2010, 2016). The Pamir interior is seismically less active, both in long-term global earthquake catalogs (Storchak et al., 2013) and observed by a dense local seismic network (Schurr et al., 2014). On 7 December 2015, a M_w7.2 strike-slip

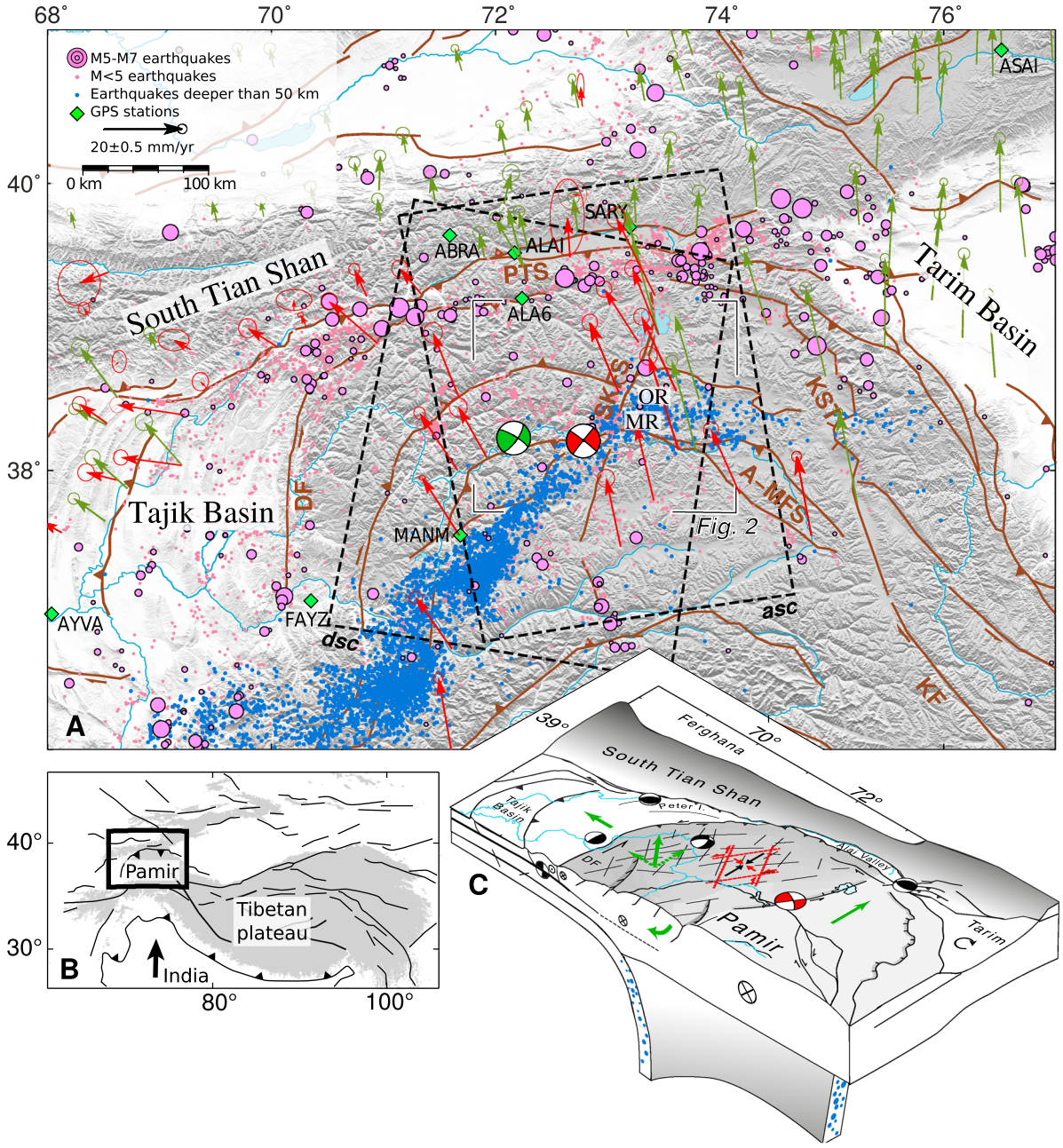

Figure 1. (a) Tectonic setting of the Pamir with main active faults (brown) (Schurr et al., 2014), microseismicity (2008–2010 and 2012–2014) (Kufner et al., 2017; Sippl, Schurr, Yuan, et al., 2013), instrumentally recorded seismicity (1900–2012) above magnitude 5 (Storchak et al., 2013), and GPS rates of Ischuk et al. (2013) (red) and Zubovich et al. (2010) (green) in a stable Eurasia reference frame. The focal mechanisms indicate the locations and mechanisms for the 1911 (green) (Kulikova et al., 2015) and the 2015 (red) earthquake (USGS, 2015). A-MFS: Aksu-Murgab fault system, DF: Darvaz fault, KF: Karakorum fault system, KST: Kongur Shan-Tashkorgan normal fault system, MR: Muzkol range, OR: Officers range, PTS: Pamir thrust system, SKFS: Sarez-Karakul fault system. (b) The Pamir and the Tibetan plateau are a result of northward advancing India (arrow). Regions above 2500 m sea level are shaded. (c) Block diagram, modified from Schurr et al. (2014), illustrating kinematics (green arrows), resulting stresses and type of faulting. The eastern Pamir is pushed north en bloc; the western Pamir deforms internally by conjugate strike-slip faulting under north-south compression, causing—together with normal faulting—westward extrusion.

earthquake occurred in the interior of the Pamir along the Sarez-Karakul fault system (SKFS) with the epicenter near Lake Sarez (Figure 1a) (Sangha et al., 2017; USGS, 2015). The earthquake killed two persons and left more than a thousand homeless. In 1911, an earthquake of similar size (M_w ~7.3) and mechanism occurred in the same region as the 2015 event (Ambraseys & Bilham, 2012; Bindi et al., 2014; Kulikova et al., 2015). This earthquake triggered a massive rockfall forming the Earth's highest dam, the Usoi dam, which confines

today's 17 km^3 Lake Sarez (Ischuk, 2006; Schuster & Alford, 2004). The proximity and similarities in mechanism and size of the two earthquakes (Kulikova et al., 2015) are striking and the question arises if the 2015 event repeated the 1911 earthquake. Herein, we present an analysis of fault location, geometry, slip distribution, and amplitude of the 2015 earthquake based on space-geodetic and field data. We discuss model parameter uncertainties and fault model resolution and compare our findings to geomorphologic near-field observations acquired 9 months after the earthquake. Finally, we interpret both earthquakes in the framework of the late Cenozoic tectonics of the Pamir.

2. Tectonic Setting

The crust of both Tibet and Pamir formed by the accretion of microcontinents, arcs, and subduction-accretion complexes to Asia's southern margin during the Paleozoic and Mesozoic (Schwab et al., 2004). During the late Miocene (~12–11 Ma), the Pamir began indenting the lithosphere of the formerly connected Tajik-Tarim basin (Kufner et al., 2016) (Figure 1). Northward displacement and crustal shortening is accommodated along the Pamir thrust system in the north, the sinistral-transpressive Darvaz fault system in the (north)west, the dextral Aksu-Murgab and Karakorum fault systems in the southeast, and the Kongur Shan-Tashkorgan normal fault system in the Chinese Pamir, which has a weak dextral component (Chevalier et al., 2015) (Figure 1a). Plate-scale processes at depth likely drive Pamir crustal tectonics (Figure 1c). Beneath the Pamir, Asian lithosphere forms a 90° arc that is retreating northward and westward as traced by intermediate-depth seismicity (60–300 km, Figure 1c) (Schneider et al., 2013; Sippl, Schurr, Tympel, et al., 2013; Sippl, Schurr, Yuan, et al., 2013). Kufner et al. (2016) suggested that Asian slab retreat is forced by indentation of the Indian lithosphere, bulldozing into the cratonic lithosphere of the Tajik-Tarim basin at mantle depth.

The high recent shortening rates across the Pamir thrust system cause frequent thrust earthquakes with the 2008 M_w6.7 Nura (Sippl et al., 2014; Teshebaeva et al., 2014) and 2016 M_w6.4 Sary Tash (USGS, 2016) earthquakes being the most recent. In the Pamir interior, thrusting has ceased and the displacement field is composed of bulk northward movement combined with E-W extension (Ischuk et al., 2013; Zhou et al., 2016). The latter is driven by westward gravitational collapse of thickened Pamir plateau crust into the Tajik basin, where it causes approximately E-W shortening of the sedimentary strata of the Tajik basin above an evaporitic décollement (Nikolaev, 2002; Schurr et al., 2014; Stübner et al., 2013) (Figure 1c). Within the Pamir, the brittle crust responds to this deformation by sinistral strike-slip faulting on NE trending or conjugate planes and to a lesser degree by normal faulting on N-S striking planes contributing to N-S shortening and westward escape (Schurr et al., 2014) (Figure 1c). Distributed strike-slip faulting, particularly in the western Pamir, also takes up shear between the northward moving Pamir and the Tajik basin lithosphere. The current deformation field has not yet left a strong imprint on the structural grain of the Pamir interior. Here the only NE striking sinistral fault system, which has a clear morphological expression and is seismically active, is the transtensional SKFS that stretches from Lake Sarez to north of Lake Karakul (Figure 1) (Rutte et al., 2017; Schurr et al., 2014; Strecker et al., 1995).

The SKFS (Figure 1) is little studied in detail by field surveys. Nöth (1932) mapped the Lake Karakul depression as a horst-graben structure. Strecker et al. (1995) traced these structures southward, outlining three stages of late Cenozoic deformation. The youngest — likely active one — has right-stepping normal faults with a minimum offset of 1–2 m, cutting alluvium in the river plain south of Lake Karakul. Here unconsolidated fluvial and aeolian sands fill the hanging wall depressions. Sippl et al. (2014) suggested that the faults at the northern end of the Karakul graben interact with active deformation along the Pamir thrust system. Overall, the northern SKFS was interpreted as a horst-graben structure with dominant normal and subordinate sinistral strike-slip displacements.

Schurr et al. (2014) and Rutte et al. (2017) traced sinistral-oblique normal faulting to the eastern escarpment of the Officers range (Figure 1a), where a series of WNW dipping, en échelon range front normal faults separate a hanging wall basin at ~3700 m from a footwall range peaking at >6000 m. At the range front, sinistral-normal slip scarps mark events along the central section of the SKFS prior to the 2015 earthquake (Figures 6b and 6c in Schurr et al. (2014) and Figures 4e–4h in Rutte et al. (2017)). The southern segments, crossing the remote Muzkol range (Figure 1a), are interpreted based on geological maps and satellite images. Structural data of late Cenozoic deformation from these studies is compiled in Figure S1 in the supporting information; these constrain the overall sinistral-oblique normal slip along the SKFS.

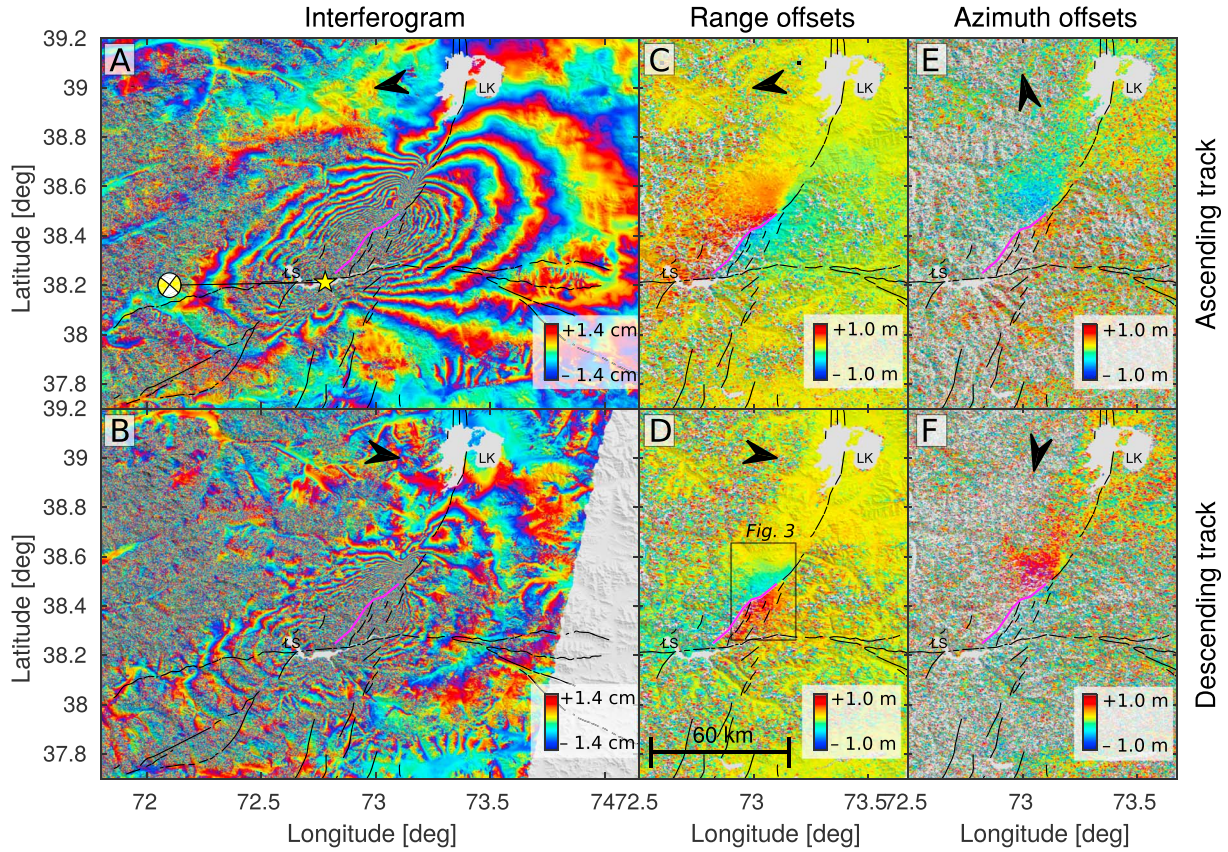

Figure 2. (a, b) Wrapped Sentinel-1A interferograms and (c, d) pixel offsets in range (i. e., line of sight) and (e, f) azimuth direction (i. e., flight direction) showing the color-coded, coseismic deformation of the 2015 Sarez earthquake. The direction of deformation is indicated in all panels by arrows, with Figures 2a–2d being also sensitive to vertical displacements. Additional features are mapped faults (black) (Schurr et al., 2014), the trace of highest deformation gradient (pink), the earthquake epicenter (yellow star), and the focal mechanism (USGS, 2015). To highlight the details near the epicenter, we only show an excerpt of the full data set that was used as model input (see Figure 1 for orientation). LK: Lake Karakul; LS: Lake Sarez.

3. Geodetic Analysis

3.1. Input Data

In this study, we use synthetic aperture radar (SAR) data from the Sentinel-1A satellite mission to extract earthquake-induced ground displacements. Displacements from SAR data are measured along the radar line-of-sight (LOS) direction as interferometric phase changes, or by cross correlation of the radar intensity signal (amplitude pixel offset tracking) along LOS and horizontally along the satellite flight direction (azimuth) (Michel & Rignot, 1999; Strozzi et al., 2002). By combining two preevent and two postevent scenes in the ascending and descending acquisition modes, we retrieved independent coseismic observations in three dimensions and complemented these observations with GPS data.

Each interferogram and pixel offset map covers a time span of 24 days (Table S1). The postevent SAR images were acquired 5 and 23 days after the earthquake, hence comprising a fraction of postseismic deformation. We concatenated two contiguous SAR scenes for each acquisition mode to cover the full surface deformation pattern and processed the data with the GAMMA software (Wegmüller & Werner, 1997). We used the 90 m digital elevation model of the shuttle radar topography mission (Farr et al., 2007; Jarvis et al., 2008) to build differential interferograms and corrected for the height-dependent, atmospheric phase contribution empirically. More details on the interferometric data processing are given in the supporting information.

The quality of the wrapped interferograms is good for the ascending and satisfactory for the descending acquisition mode (Figures 2a and 2b). Particularly, the mountainous western Pamir exhibits interferometric phase-coherence loss, probably due to snow. East of the earthquake epicenter, on the more arid eastern Pamir plateau, the interferometric phase is highly coherent but topography-related signal contributions are apparent, e.g., in the east trending valleys southeast of the epicenter. However, their short spatial wavelength

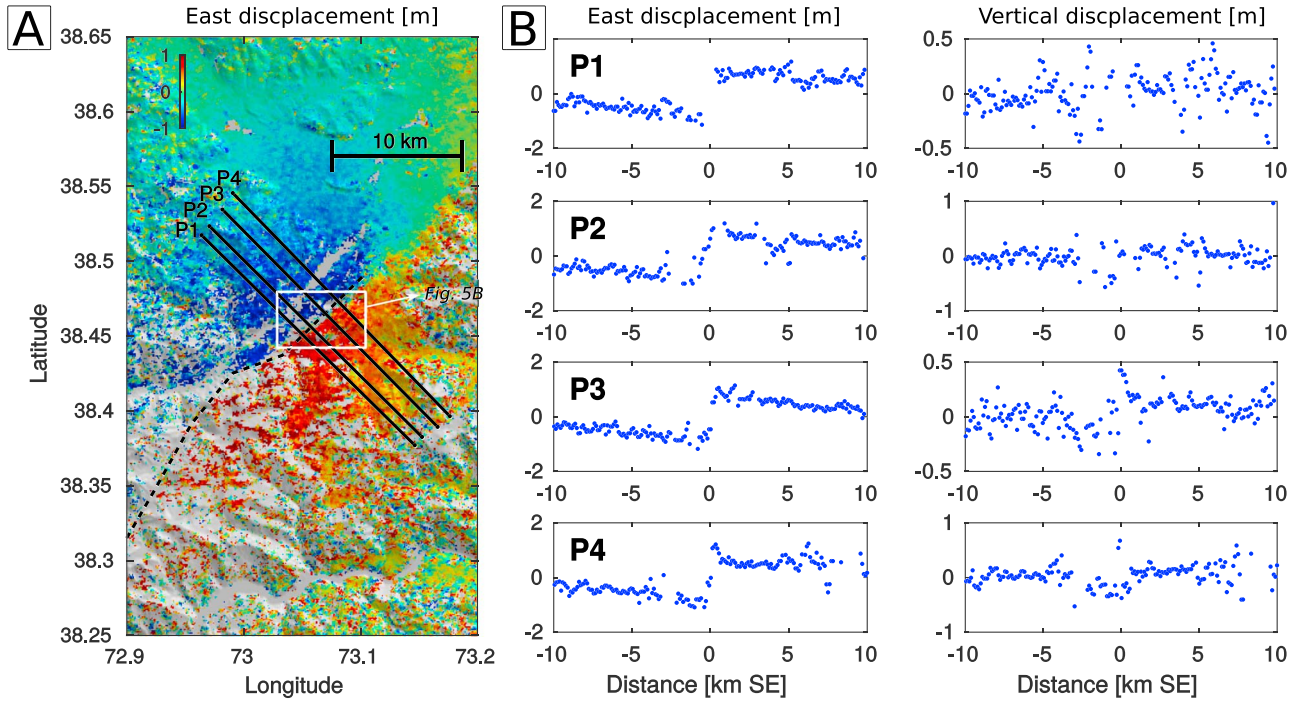

Figure 3. (a) Eastward displacement near the surface ruptures (obtained from a linear combination of Figures 2c and 2d). The dashed line marks the sign change in the data and thus the rupture surface trace. (b) Eastward and (near-)vertical displacements at the cross-fault profiles P1 to P4 (marked with black lines in Figure 3a). Each profile contains the measurements of a ~500 m wide corridor.

signals differ from the coseismic deformation pattern and do not influence the modeling results. Approaching the rupture from the undeformed area, we count more than 20 fringes on both sides of the fault. This translates to more than 56 cm of LOS displacement or over 100 cm of ground displacement (Figures 2a and 2b) on both sides, if we assume pure horizontal motion.

Displacements are highest in the near field of the rupture, where the fringe density exceeds the spatial sampling and causes interferometric phase decorrelation (Figures 2a and 2b). We unwrapped the data in a conservative fashion by masking out the near-fault area (10–20 km around the surface rupture) to prevent unwrapping errors (Figure S2). Here in the presence of large ground displacement, the pixel offset estimations deliver valuable near-fault information in range direction (i. e., LOS) and azimuth (i. e., flight direction). Given the higher spatial SAR resolution in range we average more offset estimates, which results in a better signal-to-noise ratio compared to the azimuth offsets (Figures 2c–2f). All offset data trace a sharp sign change of ~40 km length that stretches from just north of Lake Sarez northeastward toward Lake Karakul, possibly induced by a surface rupture. Eastward and near-vertical displacement profiles obtained by a linear combination of the range offsets show a relatively sharp offset of ~2 m in LOS across 1 kilometer (Figure 3). More details on the amplitude pixel offset estimation are provided in the supporting information.

Only 13 GPS markers in the Pamir region are equipped with continuously operating instruments, and they are mostly located along the active northern rim (Mohadjer et al., 2010; Schöne et al., 2013; Zubovich et al., 2016). In this study, we used the data of eight GPS stations at distances from 100 to 500 km of the epicenter (Figure 1a). The daily solutions of FAYZ and MANM were processed with GaMIT/GLOBK (Herring et al., 2010a, 2010b, 2010c); the (1 Hz) data of the other stations were analyzed with the Precise Point Positioning (PPP) software from the Canadian Spatial Reference System (CSRS) (Kouba & Héroux, 2001). Only the stations ALA6 and MANM observed a measurable coseismic displacement (Table S2 and Figure S3); all other stations are located outside the deformed area. In the modeling, we used these results as maximum constraints on the coseismically affected area. Further details on the GPS data processing are given in the supporting information.

3.2. Modeling

All SAR data were subsampled based on the phase gradient, following Jónsson et al. (2002) (Figure S2). The position of each subsampled cell was defined by the center of mass (of all coherent data samples within the cell) rather than the geometrical center. Each cell was given a weight based on the data error calculated with a full variance-covariance matrix (Figure S4) (Sudhaus & Jónsson, 2009) (we refer to the supporting information for more information). For the GPS offset data, we estimated the uncertainties based on the standard deviations of the time series and used their inverse as weights (Table S2). The distributed slip model was obtained in a two-step procedure. First, we constrained the fault location and geometry, using a nonlinear optimization routine. The amplitude pixel offsets show a clear double bend of the fault surface trace (Figures 2c–2f), so we solved for a geometry of three fault segments. Then, we linearly inverted for a variable slip on discretized fault patches, using rectangular dislocations in an elastic half-space (Okada, 1985) with a Poisson's ratio of 0.25 and an empirically derived smoothing factor resulting from a trade-off curve between data fit and maximum slip (see Figure S5 and the supporting information for further explanations). We tested two different fault-patch resolutions, namely, a uniform and a data distribution driven one. Finally, we estimated the model parameter uncertainties by propagating the data uncertainties through both the nonlinear geometry optimization and the linear slip inversion.

To constrain the fault geometry, we used a Monte Carlo type, simulated annealing approach (Cervelli et al., 2001) that first samples the model space in a random fashion and then gradually favors model parameter sets producing low misfits (Creutz, 1980; Metropolis et al., 1953). We solved for the parameters that define size, position, orientation, and lateral slip of the three fault segments and included six parameters controlling the phase ambiguity and potential tilt signal of the interferograms due to imprecise satellite-orbit information. We constrained the segments to connect at the up-dip end but all other parameters could converge freely within the given boundaries. Finally, we estimated the model geometry uncertainties by propagating the data—including a random manifestation of the data uncertainties—500 times through the optimization and performed statistics on the outcome (Figures S6 and S7) (Metzger et al., 2011; Metzger & Jónsson, 2014). The resulting best fit fault geometry contains a central fault segment of $18.5^{+0.2}_{-2.8}$ km length with a strike of $047.6^{+2.0^\circ}_{-0.0^\circ}$. It is bounded by a northeastern segment with a length of $23.8^{+0.9}_{-0.8}$ km and a strike of $025.6^{+0.7^\circ}_{-0.6^\circ}$, and a southwestern segment with a length of $23.5^{+2.4}_{-0.2}$ km and strike of $037.4^{+0.1^\circ}_{-0.3^\circ}$ (Table S3). Our solution agrees well with the fault model of Sangha et al. (2017) (Figure S6), except that all our model segments dip more steeply. In addition to the Sentinel-1 interferograms presented here, Sangha et al. (2017) included three interferometric pairs from the ALOS-2 mission. The longer wavelength (L band) of ALOS-2 provides valuable near-field information, similar to the pixel offset data used in this study. From SW to NE, our segments dip $87.7^{+1.3^\circ}_{-0.8^\circ}$ northwest, $81.8^{+0.9^\circ}_{-3.0^\circ}$ northwest, and $89.3^{+0.9}_{-1.1}$ southeast; those of Sangha et al. (2017) $89.0^{+2.3^\circ}_{-6.8^\circ}$ southeast, $80^{+9.3^\circ}_{-7.2^\circ}$ northwest, and $83^{+8.2^\circ}_{-3.5^\circ}$ northwest.

To constrain the fault slip distribution, we first extended the modeled fault planes vertically from 0 to 60 km and elongated the outer two segments north and south for 60 km in order to capture the full slip pattern. Then, we partitioned the three fault segments using two different approaches: (1) 336 uniform subpatches of 5 × 5 km width and length (4.6 × 5 km for the central fault segment) and (2) 284 subpatches subdivided optimally with respect to their data sensitivity (Atzori & Antonioli, 2009). This subdivision process relies on three criteria, that is, patch depth, data coverage, and presence of adjacent patches that already have passed the optimum resolution threshold. In addition, we constrained the patch size to be in the limits of 1–25 km. This data-driven, "optimal-patch" resolution allows only as much detail as can be resolved by the data and thus aims at suppressing artifacts (Page et al., 2009). We inverted for the slip on each of these patches, allowing for slip with a rake of ±45° only. We again solved for the best parameters representing SAR phase ambiguities and orbital signal components. The slip parameter uncertainties were estimated statistically by inverting slip on the 500 perturbed geometry realizations of the prior optimization approach (Figure S7 and text in the supporting information). Atmospheric signal contributions in the southwestern corner of the ascending interferogram would cause a significant amount of slip on the lower southwestern corner of the rupture plane. Therefore, we set the slip on the deepest patches to zero. For the optimal-patch resolution, this means that only slip above 30 km was allowed, which is in agreement with the thickness of the seismogenic layer in the Pamir (Schurr et al., 2014).

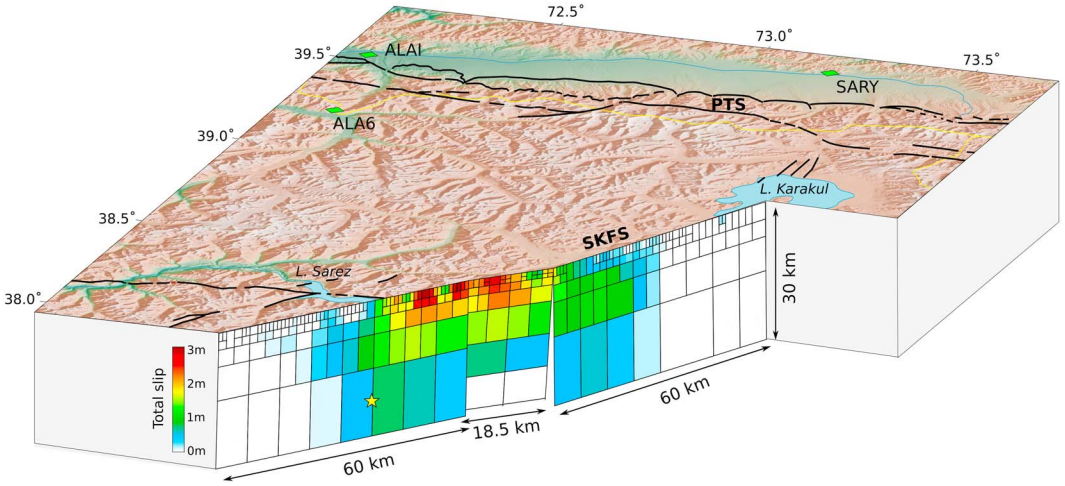

Figure 4. Perspective view on the fault-rupture plane with color-coded slip magnitudes. Mapped faults are shown in black (Schurr et al., 2014), the star marks the 2015 hypocenter (USGS, 2015), and green diamonds the closest GPS stations. We refer to Figure S8 for the rakes of the slip patches. PTS: Pamir thrust system; SKFS: Sarez-Karakul fault system.

Both slip model parameterizations reveal significant fault slip (>50 cm) on an 80 km long fault from ~25 to 30 km depth to the surface (Figures 4 and S8). Slip >2 m is confined to the upper 7.5 km of the crust (10 km for the uniform-patch slip model) along a 30 km stretch; the maximum slip is 3.1 m (2.5 m). This is less than the 4.3 m maximum along-strike slip from Landsat-8 offset estimations and less than the maximum modeled slip (3.5 m) observed by Sangha et al. (2017). The slip sense is sinistral with a minor dip-slip component at the southwestern and northeastern end of the rupture (Figure S8).

The model of Sangha et al. (2017) and our uniform and our data-driven patch slip model all show a similar slip pattern (Figure S8), but the derived slip parameter uncertainties highlight the strength of the data-driven patch resolution. The slip parameter uncertainties are generally lower and depth independent. For the uniform-patch model, the slip uncertainties are highest at deep patches, where the fault-patch resolution is suboptimal. These patches are most distant to the data samples; their patch size should be increased. Accordingly, shallow patches could be subdivided further (Figure S8). Hence, we favor the data-driven patch partitioning to the common-practice uniform fault patches. The misfit between data and modeled predictions (Figure S9) average into root-mean-square (RMS) values of 4.7 ± 0.1 cm (data-driven patches) and 4.9 ± 0.1 cm (uniform patches), respectively.

Some signal characteristics could not be reproduced, for example, the long-wavelength signal in the northeastern corner of the ascending interferogram and various areas in the descending interferogram, which were probably caused by turbulent atmospheric conditions (Figure S9). Given the poor quality of the descending amplitude pixel offsets (Figure S4), it was anticipated that the model struggles to reproduce these data well.

The total slip is equal to a seismic moment M_0 of $6.2 \pm 0.2 \cdot 10^{19}$ Nm (data-driven patches) and $5.7 \pm 0.1 \cdot 10^{19}$ Nm (uniform patches), which are equal to moment magnitudes $M_w 7.12 \pm 0.01$ and $M_w 7.10 \pm 0.01$, respectively. Both of our modeled seismic moments are slightly smaller than the results from the global seismic moment tensor inversion ($7.8 \cdot 10^{19}$ Nm of the Global Centroid Moment Tensor catalog, $10.1 \cdot 10^{19}$ Nm, USGS, 2015) and from the study of Sangha et al. (2017) ($13.7 \cdot 10^{19}$ Nm).

4. Surface Expression From Field Data: Structural Features and Their Interpretation

Field studies of surface expressions of the 2015 earthquake north of Lake Sarez are difficult to execute due to the remoteness of the glaciated Muzkol range (Figure 1a). We accessed the northern segment of the rupture, which exhibited lower slip in our model compared to the two southern segments (Figure 4). Our field studies at the southwestern tip of the Officers range (Figure 1a) aimed on mapping earthquake-related surface breaks and possible precursors, addressing fault reactivation versus neoformed breaks, fault geometry, kinematics, and coseismic offsets. Because the previous work (Rutte et al., 2017; Schurr et al., 2014; Strecker et al., 1995) indicated regional en échelon fault segmentation, we further aimed to determine the tips of one

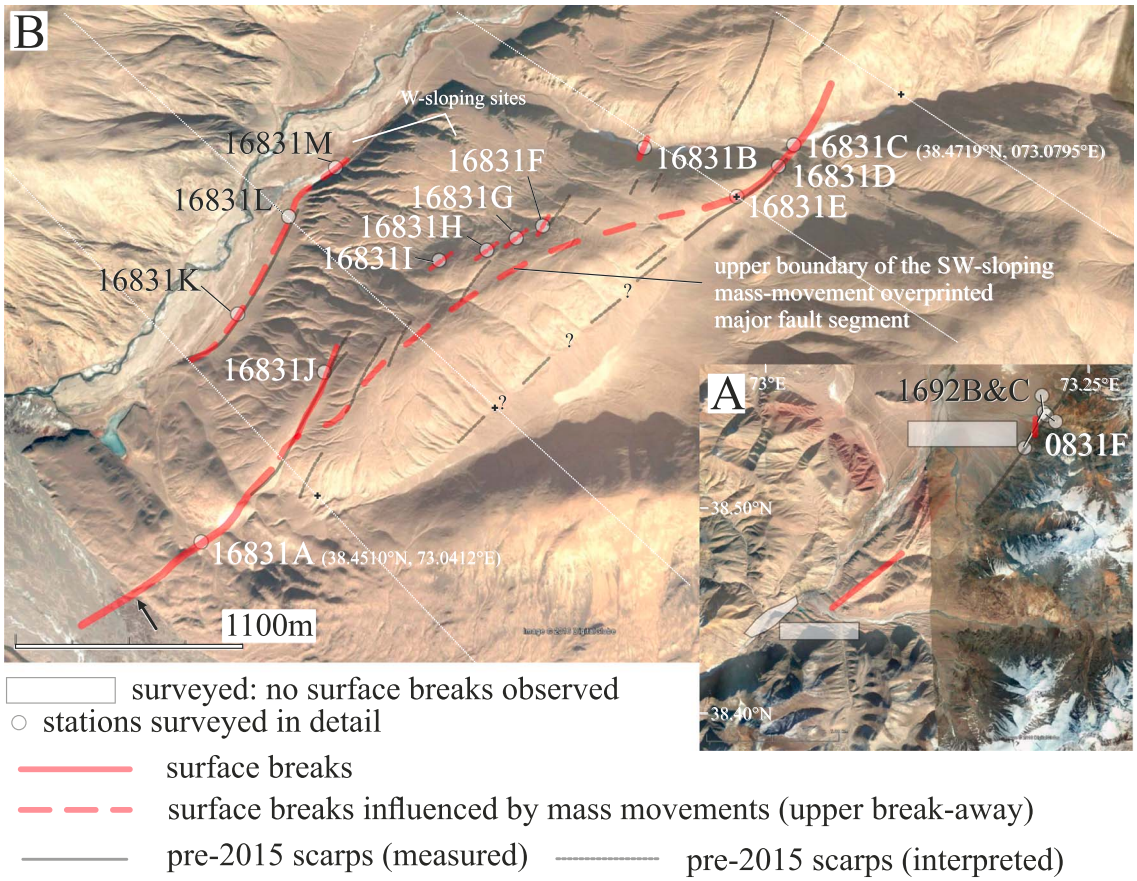

Figure 5. Overview map of (a) field observations including (b) site locations. Images from Google Earth. In Figure 5b we provide coordinates for the two key sites 16831A and 16831C (see Figure 6). The black arrow in the lower left corner marks an apparent riverbank offset. The approximately NW trending white lines are the across-fault amplitude pixel offset tracking profiles shown in Figure 3, and the black crosses on these lines mark the best estimates for the 2015 rupture trace.

segment of the 2015 event to verify its segmentation. As this event affected frozen ground, another goal was the understanding of secondary effects, that is how far liquefaction-inducing mass movements affected earthquake-induced features.

The studied area (Figure 5a) colocates with the southern 15 km of the northeastern fault model segment with near-surface slip of to 1–2 m (Figure 4) and a steep, 2 m gradient in the E-W direction across the SAR amplitude pixel offset data (Figure 3). We mapped surface breaks characterized by a right-stepping geometry indicating sinistral strike-slip displacement on the bulk structure. At sites 16831A and 16831C (Figures 5 and 6), the surface breaks cross alluvial fan deposits on subhorizontal ground, making gravitationally induced ground motion overprint unlikely. The structures at these sites (Figure 6) are en échelon secondary fractures that show sinistral offset of small-scale alluvial channels and levees and are characteristically connecting open tension fractures. The latter are mostly longer than the strike-slip fractures. The mean orientations of these secondary structures are similar between these sites (separated by ~3.7 km). The in-site orientation variability is ~45°, with pure-tension fractures and others with a measured or assumed strike-slip component. The fracture walls are uneven and reach up to 1.5 m deep (e.g., image top right in Figure 6a). When crossing vegetated creek beds (e.g., Figure 6c), identical small-scale segmentation is observed. Subordinate features are pressure ridges (≤0.5 m high, Figures 6a and 6c), again arranged en échelon, and rare antithetic fractures. We measured the trend of the enveloping surfaces of the largest en échelon secondary features, which likely approximates the orientation of the underlying primary fault. The ~045° trend is similar at both sites, ~019° off the model-determined trend of ~026°, which is better reflected by the mean trend of the secondary features (Figures 6a to 6c). At the southern end of site 16831C, the fault zone narrows and offsets a levee ridge by ~2 m, providing the best field-based offset estimate.

At the northern end of site 16831A, the surface breaks run into a hillside where earthquake-induced mass movements expose grayish-black fault gouge of a preexisting fault zone. Southwest of this site, the riverbank appears sinistrally offset by ~30 m on both sides. On the orographic right riverbank (black arrow in Figure 5b), the terrane promontory caused damming and a vegetated floodplain. The only traces of the 2015 event are several meters long fissures with a few centimeters of E-W opening; there are no surface breaks on the orographic left side and on the hilly terrane farther southwest. This "offset" either marks an erosional feature or pre-2015 events; we favor the latter, as this riverbank offset is along strike of the gouge zone observed in 16831A. At site 16831C, we mapped the ~10 m wide zone of surface breaks southwestward up a hillslope (Figure S10a, subsite 1), where it narrows to less than one meter and reactivates a preexisting fault zone that cuts consolidated moraine and alluvial fan material and forming a scarp. Slickenlines on different faces of the polished master fault allow the calculation of the reduced stress tensor (e.g., Angelier, 1984), revealing a strike-slip solution with a ~35° trending fault plane, similar to the modeled 2015 fault plane. Sites 1692B and 1692C characterize the northernmost surface breaks of the 2015 earthquake. These comprise a few meters long, ~N trending tension fractures with sinistral strike-slip offset of a few centimeters in horizontal gravelly riverbank deposits (Figure S10b). An ~2 m high, pre-2015, ~NE trending scarp was not reactivated. The piedmont-hillslope transition, partly comprising moraine material, shows several en échelon fractures, some >10 m long and with up to 0.5 m wide dilatant offset that are likely gravitational mass flow controlled. Farther north, where Schurr et al. (2014) and Rutte et al. (2017) mapped pre-2015 range front faults, we did not find surface breaks.

Sites 16831E to 16831J (Figures 5b and S10c) characterize mass movement overprinted fault segments west of the main, continuous zone of surface breaks. Although these sites show the typical en échelon arrangement of tensional fractures, they are shorter and wider than those on the horizontal sites and are characteristically downhill concave. At least sites 16831F and 16831J follow older gouge zones. Sites 16831K to 16831M (Figures 5b and S10c) are on an abandoned riverbank above the recent one and mark the westernmost observed surface breaks. The structures at these sites reactivate down-to-the-west, prerecent scarps that can be traced across alluvial fans on pre-2015 Google Earth imagery. The strike of the 2015 features, dominantly pure-tension fractures with up to 0.75 m displacement, but also including en échelon strike-slip and transtensional segments, is approximately NNE and parallel to the riverbank edge; we suspect a mass movement overprint.

Figure 5b summarizes the structures that are expected to be initiated in cohesive material by a small increment of regional shear strain along an approximately NW trending sinistral strike-slip zone. The mapped surface breaks resemble this idealized structural inventory. In our natural case, antithetic strike-slip faults are nearly absent and the secondary structures show a large orientation variation. We attribute the latter mostly to the difficulty to discriminate tensional from strike-slip faults and possibly to rotation during progressive deformation. The mapping shows that the 2015 earthquake created an array of surface breaks compatible with the focal mechanism (Figure 1a) (USGS, 2015) and the geodetically derived fault slip model (Figure 4); they outline a sinistral strike-slip fault zone characterized by segmentation. No primary surface breaks—parallel to the inferred major fault trend—are developed, but the envelope of the secondary features (marked as primary in Figure 6) likely approximates the trend of underlying fault zone. Clearly, the 2015 surface rupture reactivated preexisting faults. The field-derived offset of ≤2 m agrees with the observed SAR amplitude pixel offsets (Figure 3). Short-time liquefaction of the frozen ground facilitated the overprint of earthquake-induced structures by gravitationally induced mass movements across a zone much wider than the actual rupture.

Figure 6. Details of the field observations. (a) Site 16831A (see Figure 5b for location and coordinates). The dominant structures are en échelon secondary fractures that show sinistral offset of small-scale alluvial surface morphology. They are characteristically connecting open fractures (top right). These tension fractures are mostly longer than the strike-slip fractures (bottom right), and the fracture walls are uneven and reach up to 1.5 m deep (top right). Pressure ridges are uncommon (top left). Structures are plotted as great circles in lower hemisphere, equal area stereoplots. (b) Idealized summary of structures expected to be initiated in cohesive material by a small increment of regional shear strain along an approximately NW trending sinistral strike-slip zone. The mapped surface breaks resemble this idealized structural inventory. (c) Sites 16831B and 16831C (see Figure 5b for location and coordinates). Vegetated creek beds show identical small-scale segmentation of structures as alluvial fan deposits. The fractures cut grass and small bushes and their root network razor sharp, emphasizing displacement under frozen-ground conditions. Pressure ridges (top right) are arranged en échelon.

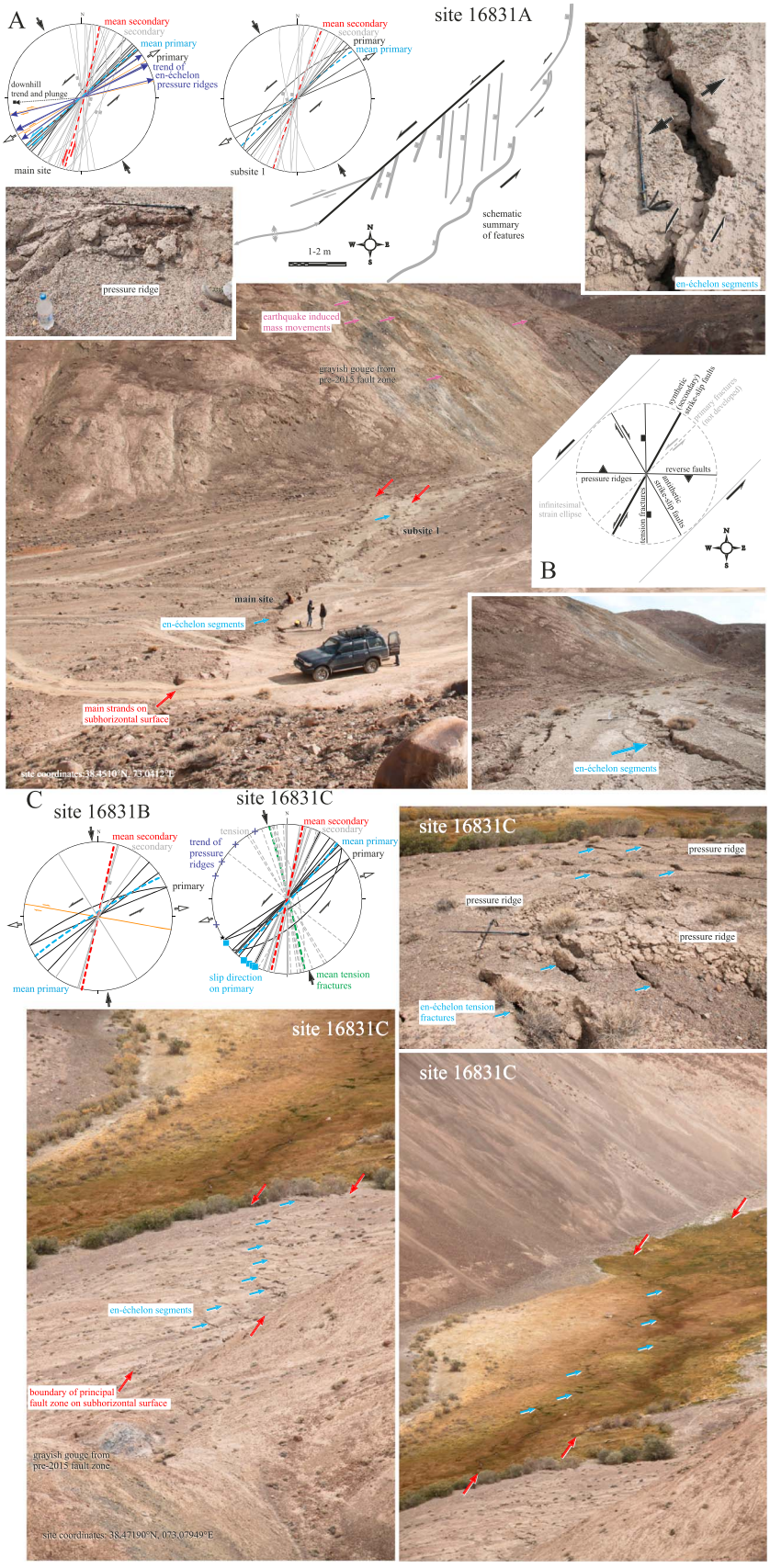

Figure 6. (continued)

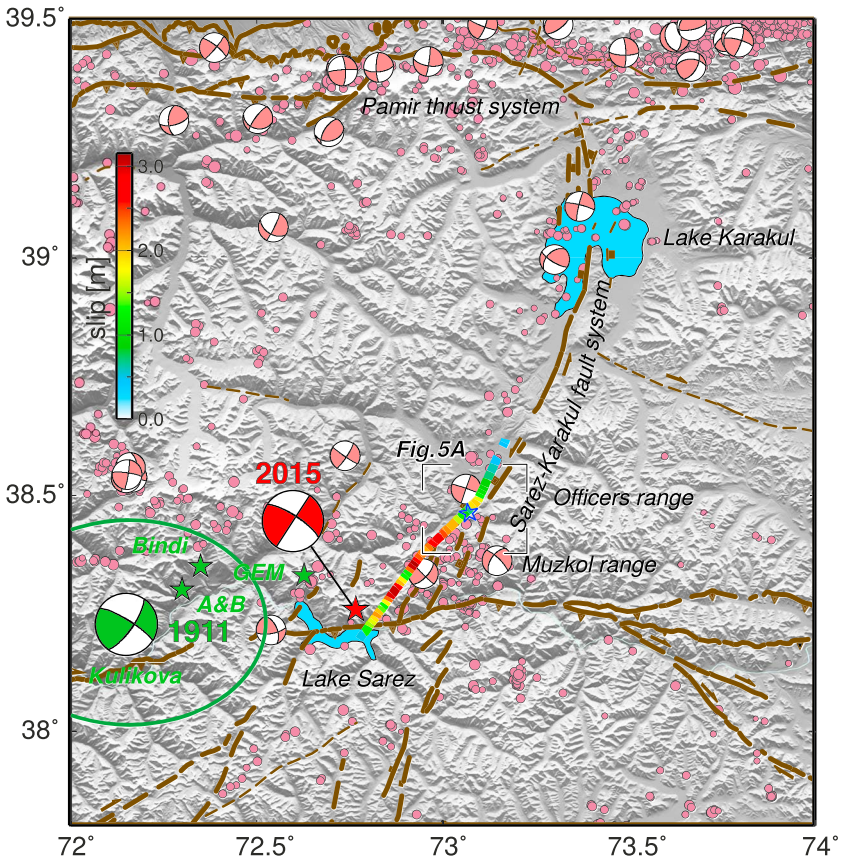

Figure 7. Close-up of the Sarez-Karakul fault system including shallow seismicity (2008–2010 and 2012–2014, purple) (Kufner et al., 2017; Sippl, Schurr, Yuan, et al., 2013), main active faults in brown, focal mechanisms of selected earthquakes in pink (Schurr et al., 2014), the 1911 event in green (Ambraseys & Bilham, 2012; Bindi et al., 2014; Kulikova et al., 2015; Storchak et al., 2013), and the 2015 earthquake in red (USGS, 2015). The color-coded line represents the modeled slip of the 2015 earthquake in the upper 2.5 km of the crust (only slip >0.5 m is shown). The inner frame marks the area of the field observations (Figure 5a), and the blue star (near 73.1°E/38.4°N) highlights the fault offset measurements discussed in section 4 and Figure 5b.

5. Discussion

The 2015 Sarez earthquake rupture appears to have initiated near Lake Sarez based on estimates of its epicenter. It then spreads northeastward crossing the Muzkol range and tapered out between Lake Sarez and Karakul (Figure 7). Seismic back projection of high-frequency emitters confirms the rupture direction (Sangha et al., 2017). Our preferred slip model exhibits highest displacements in the uppermost ~5 km. This is in contrast to other large strike-slip earthquakes (e.g., 1992 Landers and 1999 Hector Mine, California, USA, and 2003 Bam, Iran), which exhibited a slip deficit in the upper few kilometers of the fault (Fialko et al., 2005), possibly due to off-fault inelastic deformation. The amount of slip deficit scales with low values of rock cohesion in dynamic models (Kaneko & Fialko, 2011). Low cohesion occurs, for example, in the damage zone surrounding a fault core. The fact that the southern and central segments of the 2015 rupture—where we modeled the largest offsets—broke midcrustal crystalline rocks, which make up the currently exposed crust of the Muzkol range (Rutte et al., 2017), may have promoted slip reaching the surface. However, whether the earthquake broke the surface and occurred in pristine rocks along these two segments is still unclear, because this part of the rupture was not accessible in our field reconnaissance. The northeastern segment, where we made our field observation, likely is different. There, weakly to nonmetamorphic upper crustal rocks crop out, and we observed preexisting fault zones (gouge, pre-2015 scarps) nearly along the entire rupture. Characteristically, the modeled total slip increases downward along this segment (Figure 4). In addition, the more northerly trend of this rupture segment is akin to the bulk SKFS trend. Thus, we speculate that the preexisting SKFS structure controlled the northeastern segment of the 2015 earthquake (Figure 7).

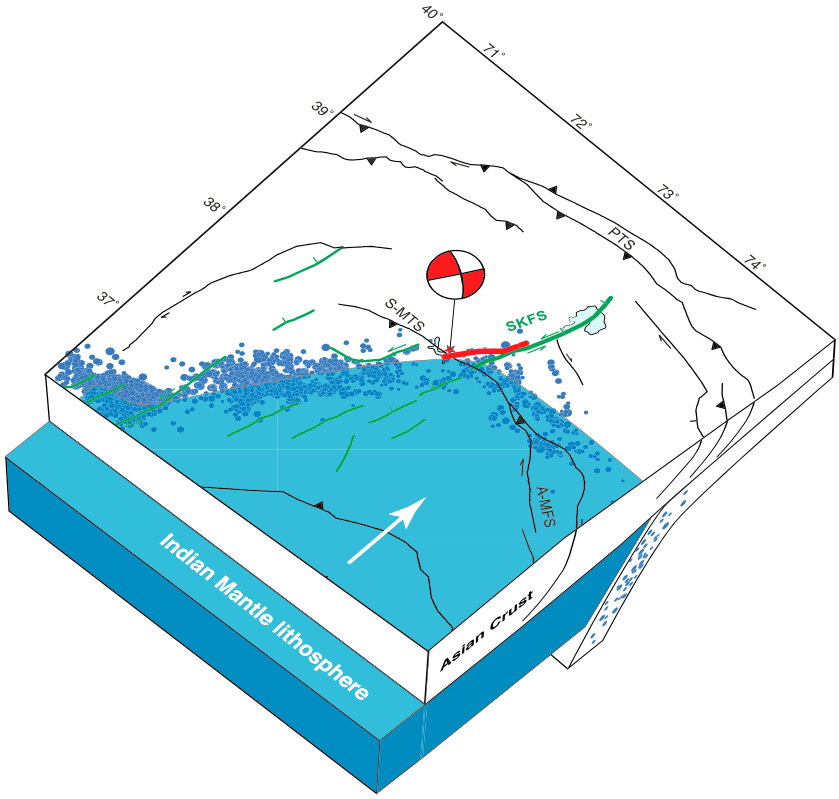

Figure 8. Perspective view of the Indian lithosphere promontory (blue) underthrusting Asian crust (white) beneath the southern and central Pamir. Intermediate-depth seismicity is marked in blue (both 2008–2010 and 2012–2014) (Kufner et al., 2017; Sippl, Schurr, Yuan, et al., 2013) and the surface projection of the rupture plane and focal mechanism of the 2015 event in red. The SKFS and faults that likely formed in the same strain field are in green. A-MFS: Aksu-Murgab fault system, PTS: Pamir thrust system, SKFS: Sarez-Karakul fault system, and S-MTS: Sarez-Murgab thrust system.

The morphologically expressed trace of the SKFS ends at the southeastern termination of the Officers range (Figure 7). Farther south, Stübner et al. (2013) and Schurr et al. (2014) mapped an array of distributed, morphologically weakly expressed, en échelon, right-stepping faults across the southwestern Pamir (Figures 1, 7, and 8). The modeled southern segment of the 2015 rupture lines up with this system of NNE to NE trending faults (Figures 7 and 8). We infer that the southern segment of the 2015 rupture is transitional to this array and connects deformation along the SKFS to the active, sinistral NNE trending faults of the Hindu Kush farther southwest (Schurr et al., 2014).

The southern end of both the 2015 rupture and the SKFS roughly coincide with a kink in the deep Pamir seismic zone where its strike changes from NE to east (Figures 1 and 8). This kink is overlain by a cluster of shallow seismicity detected during the 2008–2010 campaign (Figure 7) (Schurr et al., 2014), indicating that deformation was active there before the 2015 event.

The deep seismic zone traces the top of the delaminating and retreating Asian lithosphere between about 80 and 150 km depth (Schneider et al., 2013). According to Kufner et al. (2016), an indenter, likely the northwestern edge of the Indian lithosphere (Figure 8), molds the arc shape of this slab. The southern tip of both the 2015 Sarez rupture and the SKFS would hence coincide with the leading northwestern edge of India that has been thrusted several hundred kilometers underneath Asian crust. The NE striking fault zones traversing the Pamir may therefore be the crustal manifestation of a plate boundary at mantle depth (Schurr et al., 2014). The fault zones are thus likely accommodating displacement between Asian crust carried on top of Indian lithosphere northward and more stationary Asian crust and mantle farther west. Left-lateral shear measured with the global positioning system between the eastern Pamir and Tajik basin amounts to ~15 mm/yr (Ischuk et al., 2013). Most of this shear has been attributed to the Darvaz fault zone separating the western

Pamir and Tajik basin (Figure 1) (Ischuk et al., 2013; Trifonov, 1978). In view of the two most recent large earthquakes, 1911 and 2015, the NE striking shear zones in the western and central Pamir may play a more important role in accommodating this shear. In this context, the 2015 Sarez rupture may be the most recent manifestation of the activation of this shear zone at the northwestern tip of indenting India.

The sign change on the pixel amplitude offset maps show that the rupture stepped right north of the Muzkol range to merge with the range front sinistral-oblique normal faults of the southern SKFS (Figures 3, 4, and 7). The approximately NE trend of the southern SKFS, as emphasized by the 2015 Sarez earthquake and the geodetic and field-based analysis, changes to an approximately north trend at Lake Karakul with increasing importance of normal faulting. We attribute this to a northward increase in the active westward motion of the Pamir plateau into the Tajik basin. This northward increasing rotational component in the westward gravitational collapse of the Pamir crust is traced by (1) (north)westward increasing seismicity (Schurr et al., 2014), (2) (north)westward increasing anticlockwise rotation derived from the GPS velocity field (e.g., Ischuk et al., 2013; Zubovich et al., 2010, 2016), (3) larger paleomagnetically derived anticlockwise rotations in the northeastern than southeastern part of the eastern Tajik basin (Thomas et al., 1994), and (4) a higher abundance of the dextral strike-slip faults along the Pamir thrust system (e.g., range front segmentation) (Sippl et al., 2014; Strecker et al., 2003) than in the Pamir interior.

In 1911, an earthquake of similar size struck the Sarez region. This raises the question of the spatiotemporal and mechanical relationship between this and the 2015 event. Analyzing digitized paper seismograms of the 1911 event, Kulikova et al. (2015) reestimated the magnitude and determined a source mechanism. With a surface wave magnitude M_s7.7 and a moment magnitude M_w7.3, this event was slightly larger than the 2015 one (M_s7.6, M_w7.2, USGS, 2015). Its mechanism was also similar to the one of the 2015 event and, considering uncertainties, could have been the same. Based on intensity reports, the 1911 event was placed slightly west of Lake Sarez (Figure 7) (Ambraseys & Bilham, 2012; Bindi et al., 2014); the instrumental Global Earthquake Model catalog (Storchak et al., 2013) placed it close to Lake Sarez. Kulikova et al. (2015) relocated the event relative to the 2015 event using absolute arrival times and arrival time differences between *P* and *S* phases. The 2015 event served as a master event that provided traveltime corrections for the historical stations. This procedure located the event ~40 km west of Lake Sarez and about 50 km west of the 2015 epicenter (Figure 7). Earthquakes of this size with rupture dimensions of ~100 km do not break intact rock but need faults of some maturity. As faults grow, they cast a stress shadow, in which parallel faulting is impeded, setting a lower limit to the separation of the events, if they occurred on separate structures. Stress drop fades at distances away from the fault somewhat smaller than fault length. This would make a rupture at the epicenter of Kulikova et al. (2015) possible, considering its separation from the 2015 event. However, the locations of the 1911 event, based on both intensities and travel times suffer from significant uncertainty due to the sparse, unevenly distributed, and low-quality data available from that time. Considering just the scatter of published epicenters, a location close to or at the 2015 epicenter seems possible.

Could the 2015 event have been a repeater of the 1911 event? The relatively low strain rates in the central Pamir are hardly enough to reload the same fault in slightly more than 100 years: Compared to average GPS rates in the West Pamir, the East Pamir block exhibits 5 $\pm$ 2 mm/yr of increased NNE motion (Figure S11). *S-P* phase arrival times measured at European stations are about 6 s less for the 1911 event compared to the 2015 event (Kulikova et al., 2015), indicating that they did not occur at the same location but that the 1911 event was closer to Europe. From a stress perspective, a location of the 1911 event contiguous north or south of the 2015 rupture would be most plausible, albeit less consistent with intensities of shaking and travel times. This question may ultimately be resolved, if a surface rupture of the 1911 event could be found. Given that nearly 10 field expeditions to the Pamir have—albeit the difficulties in accessing remote terranes—not encountered well-expressed, subrecent, NE trending fault scarps in the central Pamir except along the SKFS, we prefer to locate the 1911 event along and NW of the range front faults of the Officers range (Figure 7). This speculation would hint to a reactivation of a pre-2015 fault zone (the SKFS) and locate it along the most prominent mapped, prerecent scarps. It would place the 2015 event in an area strongly loaded by the 1911 event, and interpreting it as the most recent manifestation of the building of a continuous fault zone along the western edge of the deep Indian intender (connecting the Hindu Kush with the SKFS) (Schurr et al., 2014).

6. Conclusion

We have presented a finite-fault slip model of the 7 December 2015, M_w7.2 Sarez, Pamir, earthquake, using SAR interferometry, SAR amplitude pixel offsets, and GPS data. The earthquake ruptured on a right-stepping, ~80 km long NE trending fault, accommodating sinistral slip of up to 3.1 m in the uppermost part of the fault. Our data-distribution-driven slip-patch model showed less variance in the slip parameter uncertainties compared to a model with uniform slip patches.

The results of the geodetic modeling were compared to field observations acquired 9 months after the earthquake. Where the rupture was accessible, the field observations such as fault strike and sense and amplitude of slip agree well with what we observed in the seismic and geodetic data.

The 2015 Sarez earthquake rupture shows a compelling geometric relation to the deep Pamir earthquake zone. In a geodynamic context, we suggest that the 2015 Sarez rupture may be the most recent manifestation of a shear zone at the northwestern tip of the Indian indenter at mantle depth.

Acknowledgments
Anatoly Ischuk (Tajik Academy of Sciences), Najibullah Kakar (Norwegian Afghanistan Committee), and Alexander Zubovich (Central Asian Institute of Applied Geosciences) maintain the CGPS stations and provided the raw data. Shokhrukh Murodkulov and Sharifov Umedzhon (both Tajik Academy of Sciences) assisted during fieldwork, which was funded by GFZ. ESA Sentinel-1A SAR data are provided by the Copernicus Sentinels Scientific Data Hub (https://scihub.copernicus.eu/dhus). Simone Atzori supported us in implementing the optimal-patch resolution code. Some figures were produced using the Generic Mapping Tools (GMT) public domain software (Wessel et al., 2013).

References

Ambraseys, N., & Bilham, R. (2012). The Sarez-Pamir earthquake and landslide of 18 February 1911. *Seismological Research Letters*, *83*(2), 294–314. https://doi.org/10.1785/gssrl.83.2.294

Angelier, J. (1984). Tectonic analysis of fault-slip data sets. *Journal of Geophysical Research*, *89*(B7), 5853–5848. https://doi.org/doi:10.1029/JB089iB07p05835

Atzori, S., & Antonioli, A. (2009). Optimal fault resolution in geodetic inversion of coseismic data. *Geophysical Journal International*, *185*, 529–530. https://doi.org/10.1111/j.1365-246X.2011.04955.x

Bindi, D., Parolai, S., Gómez-Capera, A., Locatid, M., Kalmetyeva, Z., & Mikhailova, N. (2014). Locations and magnitudes of earthquakes in Central Asia from seismic intensity data. *Journal of Seismology*, *18*, 1–21. https://doi.org/10.1007/s10950-031-9392-1

Cervelli, P., Murray, M. H., Segall, P., Aoki, Y., & Kato, T. (2001). Estimating source parameters from deformation data, with an application to the March 1997 earthquake swarm off the Izu Peninsula. *Journal of Geophysical Research*, *106*(B6), 11,217–11,237. https://doi.org/10.1029/2000JB900399

Chevalier, M. L., Pan, J., Li, H., & Wang, M. (2015). Quantification of both normal and right-lateral late Quaternary activity along the Kongur Shan extensional system, Chinese Pamir. *Terra Nova*, *27*, 379–391. https://doi.org/10.1111/ter.12170

Creutz, M. (1980). Monte-Carlo study of quantized SU(2) gauge-theory. *Physical Review D: Particles and Fields*, *21*(8), 2308–2315. https://doi.org/10.1103/PhysRevD.21.2308

Farr, T. G., Rosen, P. A., Caro, E., Crippen, R., Duren, R., Hensley, S., … Alsdorf, D. (2007). The shuttle radar topography mission. *Reviews of Geophysics*, *45*, RG2004. https://doi.org/10.1029/2005RG000183

Fialko, Y., Sandwell, D., Simons, M., & Rosen, P. (2005). Three-dimensional deformation caused by the Bam, Iran, earthquake and the origin of shallow slip deficit. *Nature*, *435*(7040), 295–299. https://doi.org/10.1038/nature03425

Herring, T. A., King, R. W., & McClusky, S. C. (2010a). *GAMIT reference manual—GPS analysis at MIT, release 10.4*. Cambridge, MA: Department of Earth, Atmospheric, and Planetary Sciences, Massachusetts Institute of Technology.

Herring, T. A., King, R. W., & McClusky, S. C. (2010b). *GLOBK reference manual—Global Kalman filter VLBI and GPS analysis program, release 10.4*. Cambridge, MA: Department of Earth, Atmospheric, and Planetary Sciences, Massachusetts Institute of Technology.

Herring, T. A., King, R. W., & McClusky, S. C. (2010c). *Introduction to GAMIT/GLOBK, release 10.4*. Cambridge, MA: Department of Earth, Atmospheric, and Planetary Sciences, Massachusetts Institute of Technology.

Ischuk, A. (2006). Usoy natural dam: Problem of security; Lake Sarez, Pamir Mountains, Tadjikistan. *Italian Journal of Engineering Geology and the Environment Special Issue*, *1*, 189–192. https://doi.org/10.4408/IJEGE2006-01.S-26

Ischuk, A., Bendick, R., Rybin, A., Molnar, P., Khan, F. S., Kuzikov, S., … Zubovich, A. V. (2013). Kinematics of the Pamir and Hindu Kush regions from GPS geodesy. *Journal of Geophysical Research: Solid Earth*, *118*, 2408–2416. https://doi.org/10.1002/jgrb.50185

Jarvis, A., Reuter, H. I., Nelson, A., & Guevara, E. (2008). Hole-filled SRTM for the globe version 4. Available from the CGIAR-CSI SRTM 90 m Database http://srtm.csi.cgiar.org.

Jónsson, S., Zebker, H., Segall, P., & Amelung, F. (2002). Fault slip distribution of the 1999 M_w 7.1 Hector Mine, California, earthquake, estimated from satellite radar and GPS measurements. *Bulletin of the Seismological Society of America*, *92*(4), 1377–1389. https://doi.org/10.1785/0120000922

Kaneko, Y., & Fialko, Y. (2011). Shallow slip deficit due to large strike-slip earthquakes in dynamic rupture simulations with elasto-plastic off-fault response. *Geophysical Journal International*, *186*, 1389–1403. https://doi.org/10.1111/j.1365-246X.2011.05117.x

Kouba, J., & Héroux, P. (2001). Precise point positioning using IGS orbit and clock products. *GPS solutions*, *5*(2), 12–28. https://doi.org/10.1007/PL00012883

Kufner, S.-K., Schurr, B., Haberland, C., Zhang, Y., Saul, J., Ischuk, A., & Oimahmadov, I. (2017). Zooming into the Hindu Kush slab break-off: A rare glimpse on the terminal stage of subduction. *Earth and Planetary Science Letters*, *461*, 127–140. https://doi.org/10.1016/j.epsl.2016.12.043

Kufner, S.-K., Schurr, B., Sippl, C., Yuan, X., Ratschbacher, L., Akbar, A. s/of Mohammad, … Tilmann, F. (2016). Deep India meets deep Asia: Lithospheric indentation, delamination and break-off under Pamir and Hindu Kush, Central Asia. *Earth and Planetary Science Letters*, *435*, 171–184. https://doi.org/10.1016/j.epsl.2015.11.046

Kulikova, G., Schurr, B., Krüger, F., Brzoska, E., & Heimann, S. (2015). Source parameters of the Sarez-Pamir earthquake of 1911 February 18. *Geophysical Journal International*, *205*(2), 1086–1098. https://doi.org/10.1093/gji/ggw069

Metropolis, N., Rosenbluth, A. W., Rosenbluth, M. N., Teller, A. H., & Teller, E. (1953). Equation of state calculations by fast computing machines. *Journal of Chemical Physics*, *21*(6), 1087–1092. https://doi.org/10.1063/1.1699114

Metzger, S., & Jónsson, S. (2014). Plate boundary deformation in North Iceland during 1992–2009 revealed by InSAR time-series analysis and GPS. *Tectonophysics*, *634*, 127–138. https://doi.org/10.1016/j.tecto.2014.07.027

Metzger, S., Jónsson, S., & Geirsson, H. (2011). Locking depth and slip-rate of the Husavík Flatey fault, North Iceland, derived from continuous GPS data 2006–2010. *Geophysical Journal International*, *187*(2), 564–576. https://doi.org/10.1111/j.1365-246X.2011.05176.x

Michel, R., & Rignot, E. (1999). Flow of Glaciar Moreno, Argentina, from repeat-pass Shuttle Imaging Radar images: Comparison of the phase correlation method with radar interferometry. *Journal Glaciology*, *45*(149), 93–100. https://doi.org/10.1017/S0022143000003075

Mohadjer, S., Bendick, S. R., Ischuk, A., Kuzikov, S., Kostuk, A., Saydullaev, U., … Zubovich, A. V. (2010). Partitioning of India/Eurasia convergence in the Pamir-Hindu Kush from GPS measurements. *Geophysical Research Letters*, *37*, L04305. https://doi.org/10.1029/2009GL041737

Nikolaev, V. (2002). Afghan-Tajik depression: Architecture of sedimentary cover and evolution. *Russian Journal of Earth Sciences*, *4*(6), 399–421. https://doi.org/10.2205/2002ES000106

Nöth, L. (1932). Geologische Untersuchungen im nordwestlichen Pamirgebiet und mittleren Transalai. In H. V. Ficker & W. Rickmers (Eds.), *Wissenschaftliche ergebnisse der Alai-Pamir expedition 1928, Teil II*. Berlin: Reimer-Vohsen.

Okada, Y. (1985). Surface deformation due to shear and tensile faults in a half-space. *Bulletin of the Seismological Society of America*, *75*(4), 1135–1154.

Page, M. T., Custódio, S., Archuleta, R., & Carlson, J. M. (2009). Constraining earthquake source inversions with GPS data: 1. Resolution-based removal of artifacts. *Journal of Geophysical Research*, *114*, B01314. https://doi.org/10.1029/2007JB005449

Rutte, D., Ratschbacher, L., Schneider, S., Stübner, K., Stearns, M. A., Gulzar, M. A., & Hacker, B. R. (2017). Building the Pamir-Tibet Plateau—Crustal stacking, extensional collapse, and lateral extrusion in the Central Pamir: 1. Geometry and kinematics. *Tectonics*, *36*, 342–384. https://doi.org/10.1002/2016TC004293

Sangha, S., Peltzer, G., Zhang, A., Meng, L., Lian, C., Lundgren, P., & Fielding, E. (2017). Fault geometry of 2015, M_w7.2 Murghab, Tajikistan earthquake controls rupture propagation: Insights from InSAR and seismological data. *Earth and Planetary Science Letters*, *462*, 132–141. https://doi.org/10.1016/j.epsl.2017.01.018

Schneider, F. M., Yuan, X., Schurr, B., Mechie, J., Sippl, C., Haberland, C., … Negmatullaev, S. (2013). Seismic imaging of subducting continental lower crust beneath the Pamir. *Earth and Planetary Science Letters*, *375*, 101–112. https://doi.org/10.1016/j.epsl.2013.05.015

Schöne, T., Zech, C., Unger-Shayesteh, K., Rudenko, V., Thoss, H., Wetzel, H.-U., … Zubovich, A. (2013). A new permanent multi-parameter monitoring network in Central Asian high mountains—From measurements to data bases. *Geoscience Instrumentation Methods Data Systems*, *2*, 97–111. https://doi.org/10.5194/gid-2-301-2012

Schurr, B., Ratschbacher, L., Sippl, C., Gloaguen, R., Yuan, X., & Mechie, J. (2014). Seismotectonics of the Pamir. *Tectonics*, *33*(8), 1501–1518. https://doi.org/10.1002/2014TC003576

Schuster, R. L., & Alford, D. (2004). Usoi landslide dam and Lake Sarez, Pamir Mountains, Tajikistan. *Environmental and Engineering Geoscience*, *2*, 151–168. https://doi.org/10.2113/10.2.151

Schwab, M., Ratschbacher, L., Siebel, W., McWilliams, M., Lutkov, V., Minaev, V., … Wooden, J. (2004). Assemblage of the Pamirs: Age and origin of magmatic belts from the southern Tien Shan to the southern Pamirs and their relation to Tibet. *Tectonics*, *23*, TC4002. https://doi.org/10.1029/2003TC001583

Sippl, C., Schurr, B., Tympel, J., Angiboust, S., Mechie, J., Yuan, X., … TIPAGE-Team (2013). Deep burial of Asian continental crust beneath the Pamir imaged with local earthquake tomography. *Earth and Planetary Science Letters*, *384*, 165–177. https://doi.org/10.1016/j.epsl.2013.10.013

Sippl, C., Schurr, B., Yuan, X., Mechie, J., Schneider, F. M., Gadoev, M., … Radjabov, N. (2013). Geometry of the Pamir-Hindu Kush intermediate-depth earthquake zone from local seismic data. *Journal of Geophysical Research: Solid Earth*, *118*, 1438–1457. https://doi.org/10.1002/jgrb.50128

Sippl, C., Ratschbacher, L., Schurr, B., Krumbiegel, C., Rui, H., Pingren, L., & Abdybachaev, U. (2014). The 2008 Nura earthquake sequence at the Pamir-Tian Shan collision zone, southern Kyrgyzstan. *Tectonics*, *33*(12), 2382–2399. https://doi.org/10.1002/2014TC003705

Storchak, D. A., Di Giacomo, D., Bondár, I., Engdahl, E., Harris, J., Lee, W. H. K., … Bormann, P. (2013). Public release of the ISC-GEM global instrumental earthquake catalogue (1900–2009). *Seismological Research Letters*, *84*, 810–815. https://doi.org/10.1785/0220130034

Strecker, M. R., Arrowsmith, J. R., & Coutand, I. (2003). Differential structural and geomorphic mountain-front evolution in an active continental collision zone: The northwest Pamir, southern Kyrgyzstan. *Geological Society of America Bulletin*, *115*(2), 166–181. https://doi.org/10.1130/0016-7606(2003)115<0166:DSAGMF>2.0.CO;2

Strecker, M. R., Frisch, W., Hamburger, M. W., Ratschbacher, L., Semiletkin, S., Zamoruyev, A., & Sturchio, N. (1995). Quaternary deformation in the Eastern Pamirs, Tadzhikistan and Kyrgyzstan. *Tectonics*, *14*(5), 1061–1079. https://doi.org/10.1029/95TC00927

Strozzi, T., Luckman, A., Murray, T., Wegmüller, U., & Werner, C. L. (2002). Glacier motion estimation using SAR offset-tracking procedures. *IEEE Transactions on Geoscience and Remote Sensing*, *40*(11), 2384–2391. https://doi.org/10.1109/TGRS.2002.805079

Stübner, K., Ratschbacher, L., Rutte, D., Stanek, K., Minaev, V., Wiesinger, R., … Project TIPAGE members (2013). The giant Shakhdara migmatitic gneiss dome, Pamir, India-Asia collision zone. 1: Geometry and kinematics. *Tectonics*, *32*, 948–979. https://doi.org/10.1002/tect.20057

Sudhaus, H., & Jónsson, S. (2009). Improved source modeling through combined use of InSAR and GPS under consideration of correlated data errors: Application to the June 2000 Kleifarvatn earthquake Iceland. *Geophysical Journal International*, *176*(2), 389–404. https://doi.org/10.1111/j.1365-246X.2008.03989.x

Teshebaeva, K., Sudhaus, H., Echtler, H., Schurr, B., & Roessner, S. (2014). Strain partitioning at the eastern Pamir-Alai revealed through SAR data analysis of the 2008 Nura earthquake. *Geophysical Journal International*, *198*(2), 760–774. https://doi.org/10.1093/gji/ggu158

Thomas, J., Chauvin, A., Gapais, D., Bazhenov, M., Perroud, H., Cobbold, P., & Burtman, V. (1994). Paleomagnetic evidence for Cenozoic block rotations in the Tadjik depression (Central Asia). *Journal of Geophysical Research*, *99*(B8), 15,141–15,160. https://doi.org/10.1029/94JB00901

Trifonov, V. (1978). Late Quaternary tectonic movements of western and central Asia. *Bulletin of the Geological Society America*, *89*(7), 1059–1072.

U.S. Geological Survey (USGS) (2015). *M* 7.2—104 km W of Murghob, Tajikistan (Tech. Rep.). Menlo Park, CA: US Geological Survey.

U.S. Geological Survey (USGS) (2016). *M* 6.4—28 km SSE of Sary-Tash, Kyrgyzstan (Tech. Rep.). Menlo Park, CA: US Geological Survey.

Wegmüller, U., & Werner, C. (1997). Gamma SAR processor and interferometry software. In *ERS symposium on space at the service of our environment* (pp. 1687–1692). Florence, Italy: European Space Agency.

Wessel, P., Smith, W. H. F., Scharroo, R., Luis, J. F., & Wobbe, F. (2013). Generic Mapping Tools: Improved version released. *Eos, Transactions American Geophysical Union*, *94*, 409–410. https://doi.org/10.1002/2013EO450001

Zhou, Y., He, J., Oimahmadov, I., Gadoev, M., Pan, Z., Wang, W., … Rajabov, N. (2016). Present-day crustal motion around the Pamir Plateau from GPS measurements. *Gondwana Research*, *35*, 144–154. https://doi.org/10.1016/j.gr.2016.03.011

Zubovich, A., Schöne, T., Metzger, S., Mosienko, O., Mukhamediev, S., Sharshebaev, A., & Zech, C. (2016). Tectonic interaction between the Pamir and Tien Shan observed by GPS. *Tectonics*, *35*(2), 283–292. https://doi.org/10.1002/2015TC004055

Zubovich, A. V., Wang, X.-Q., Scherba, Y. G., Schelochkov, G. G., Reilinger, R., Reigber, C., … Beisenbaev, R. T. (2010). GPS velocity field of the Tien Shan and surrounding regions. *Tectonics*, *29*, TC6014. https://doi.org/10.1029/2010TC002772